
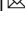







Interannual oxygen isotope variability in Indian summer monsoon precipitation reflects changes in moisture sources

Gayatri Kathayat ¹, Ashish Sinha ², Masahiro Tanoue ³, Kei Yoshimura⁴, Hanying Li¹, Haiwei Zhang¹ & Hai Cheng ^{1,5,6}

The primary influences on the spatio-temporal variability of oxygen isotope compositions in precipitation over the Indian summer monsoon domain are inadequately constrained by the limited observational record. Consequently, the climatic significance of isotopic signatures of precipitation preserved in proxy archives from the region remains unclear. Here we present simulations with an isotope-enabled climate model (IsoGSM2) with the moisture-tagging capability to investigate the role of relative contributions of moisture from oceanic and terrestrial sources to the interannual variability in oxygen isotope composition in summer monsoon rainfall. During weak monsoon years, the moisture contribution from the Arabian Sea dominates precipitation over the Indian subcontinent while the remote oceanic and terrestrial sources have a greater influence during strong monsoon years. We suggest that changes in monsoon circulation, moisture source, and precipitation intensity are interrelated and that speleothem oxygen isotope records from the region can potentially help reconstruct interannual to decadal monsoon rainfall variability.

¹Institute of Global Environmental Change, Xi'an Jiaotong University, Xi'an, China. ²Department of Earth Science, California State University, Carson, CA, USA. ³Center for Global Environmental Research, National Institute for Environmental Studies, Tsukuba, Ibaraki, Japan. ⁴Atmosphere and Ocean Research Institute, The University of Tokyo, Kashiwa, Chiba, Japan. ⁵State Key Laboratory of Loess and Quaternary Geology, Institute of Earth Environment, Chinese Academy of Sciences, Xi'an, China. ⁶Department of Earth and Environmental Sciences, University of Minnesota, Minneapolis, MN, USA.

email: kathayat@xjtu.edu.cn; asinha@csudh.edu

The oxygen isotopic signatures of precipitation ($\delta^{18}\text{O}_p$) preserved in natural archives such as ice cores, tree ring cellulose, and speleothems are widely used for reconstructing past climatic conditions. Nonetheless, the relative importance of various hydrological cycle processes in driving the spatial-temporal $\delta^{18}\text{O}_p$ variability in the Asian monsoonal regions remains inadequately constrained. A case in point is the contentious debate surrounding the climatic significance of the speleothem $\delta^{18}\text{O}$ records from the East Asian summer monsoon (EASM) region^{1–7}. The earlier (c. the 2000s) interpretations of these records focused on the role of summer monsoon “intensity” or the ratio of summer to winter precipitation in driving $\delta^{18}\text{O}$ changes on orbital timescales^{8,9}. However, as more observational $\delta^{18}\text{O}_p$ data have since become available, together with the refinements in numerical modeling of water isotopes in general circulation model (GCM)^{10–12}, the EASM $\delta^{18}\text{O}_p$ and speleothem $\delta^{18}\text{O}$ variability are now suggested to arise from “upstream” processes such as seasonal changes in circulation^{13,14}, moisture sources^{15,16}, transport history¹⁷, and not necessarily from changes in the amount of precipitation at the local or regional scale (see review in ref. 18).

In contrast to their EASM counterparts, the speleothem $\delta^{18}\text{O}$ records from the Indian summer monsoon (ISM) regions (Fig. 1; Supplementary Fig. 1 and Supplementary Note 1) have largely escaped scrutiny but key elements of these records require a critical reappraisal¹⁹. For example, some speleothem $\delta^{18}\text{O}$ records from India exhibit a rather large $\delta^{18}\text{O}$ change ($\sim 6\text{--}8\%$) across the millennial-scale abrupt climate events and glacial terminations^{20,21}, which is two to three times larger than the coeval EASM speleothem records²². If interpreted solely in the framework of changes in upstream circulation and/or moisture sources, large millennial-scale $\delta^{18}\text{O}$ shifts imply a massive reorganization of the ISM dynamics. Similarly, the late Holocene speleothem $\delta^{18}\text{O}$ records from India exhibit protracted (sub-decadal to multidecadal) intervals of extreme positive $\delta^{18}\text{O}$ anomalies ($\sim 2\text{--}3$ standard deviation excursions from the mean), which are interpreted to reflect periods of drastically reduced monsoon rainfall. Such reconstructions are, however, at odds with the ISM variability observed during the instrumental period, where there have never been more than five droughts in any continuous 10-year interval in India^{23–27}.

Previous attempts to cast the observed spatio-temporal $\delta^{18}\text{O}_p$ patterns over the Indian subcontinent in the context of changes in circulation and moisture source–transport–sink relationships have largely relied on Lagrangian models^{26,28–31}. While this approach has provided some mechanistic insights into the $\delta^{18}\text{O}_p$ variability at synoptic scales^{26,31}, its broader applications to seamlessly investigate long-term variations in moisture origin are limited by the brevity of observational $\delta^{18}\text{O}_p$ data. The Eulerian-based approach implemented within the isotope-enabled GCMs provides an alternative method to elucidate the role of moisture source dynamics on the $\delta^{18}\text{O}_p$. This method involves “tagging” water vapor from predefined regions and tracing their movement during the hydrological cycle^{32–37}. In this study, we have used an isotope-incorporated Global Spectral Model version 2 (IsoGSM2)³⁸ with water vapor-tagging capability (see “Methods”) to illustrate the relative importance of large-scale moisture transport from various oceanic and terrestrial sources in driving the interannual $\delta^{18}\text{O}_p$ variability over the Indian subcontinent. Intercomparisons with other isotope-enabled models indicate that IsoGSM2 reproduces the annual cycles in precipitation and $\delta^{18}\text{O}_p$ over the ISM³⁹ and EASM regions⁷, arguably, with the highest fidelity. Importantly, the model simulates the intra-seasonal to interannual variability in $\delta^{18}\text{O}_p$ over the Indian subcontinent with high fidelity, which is directly comparable to the observational data (Supplementary Figs. 2–5; Supplementary Table 1,

“Methods”), indicating that IsoGSM2 has high skill in reproducing moisture transport processes and hydrological cycle over the ISM domain.

Results

Regional setting. The onset of summer monsoon rainfall over the Indian subcontinent is marked by the development and intensification of cross-equatorial low-level jet (LLJ). The LLJ with a core at the height of ~ 1.5 km (corresponding to ~ 850 hPa level), is the dominant pathway of moisture transport across the equatorial Indian Ocean and the Arabian Sea onto the Indian landmass¹ (Supplementary Fig. 1). The LLJ induces strong cyclonic vorticity in the planetary boundary layer over central India that leads to moisture convergence and the formation of the monsoon trough (MT across central India to the Bay of Bengal (BoB) (e.g., ref. 41). After exiting India, the LLJ reconstitutes over the northern BoB, turning into a southeasterly flow, transporting moisture to eastern and northeastern India, and occasionally as far northwest as Pakistan. Besides these two moisture transport pathways, the negative pressure anomalies over the MT draw synoptic-scale low-pressure systems (LPS) from the BoB⁴², which further transport oceanic vapor across central to northwest India. The LLJ mediated moisture transport has been shown to vary on both intraseasonal to interannual timescales^{43–45}. Typically, during weaker monsoon, moisture transport along the LLJ climatological axis ($\sim 15^\circ\text{N}$) weakens and the LLJ also morphs into two branches, with one branch passing south of India and the other passes through north India, with its core at $\sim 25^\circ\text{N}$ (Supplementary Fig. 1)⁴⁰.

Tagging design. In this study, we tagged moisture from the following source regions: (1) The Bay of Bengal (BoB), (2) the Arabian Sea (including the Red Sea and the Gulf of Oman (hereafter, ARAB), (3) northern Indian Ocean (NIO), (4) southern Indian Ocean (SIO), (5) the western part of the Pacific Ocean (PCO), and (6) land surfaces (LND) (Fig. 1a). The atmospheric column precipitable water derived from tagged regions was used to identify the source region of the water vapor. Comparisons with climatological values of vertically integrated moisture flux divergence using the Fifth Generation European Centre for Medium-Range Weather Forecasts Reanalysis (ERA-5) suggests that our tagged moisture source regions encompass all potential sources of oceanic moisture based on the E–P threshold of 400 mm/season (Supplementary Fig. 6)^{46,47}. The climatological contributions of moisture from each tagged region were evaluated over a common “sink” region over central India ($\sim 15^\circ\text{N}$ to 28°N and $70\text{--}94^\circ\text{E}$), commonly referred to as the core monsoon zone (CMZ)⁴⁸. The moisture contributions to three additional sink regions ($4^\circ \times 4^\circ$ area centered over each of the proxy site locations) in north, northeast, and central India were also assessed (Supplementary Fig. 1c). The combined contributions of moisture originating from all six tagged sources to the total precipitable water (TPW) over the CMZ (Fig. 1c) and other sinks range between 96 and 100% during the pre-monsoon (April–May), monsoon (JJAS), and post-monsoon (October) seasons, indicating that the identified moisture source regions adequately represent the dominant sources of precipitation at each of our sink regions (Supplementary Fig. 7). Extensive validation of model-simulated isotope data including reproducing the observed interannual, seasonal, and intra-seasonal variations in $\delta^{18}\text{O}_p$ ⁴⁹ suggests that IsoGSM2 has high skill in reproducing moisture transport processes and hydrological cycle over the ISM domain.

Climatology of moisture contributions. The annual cycles in simulated moisture contributions to the TPW (longitudinally

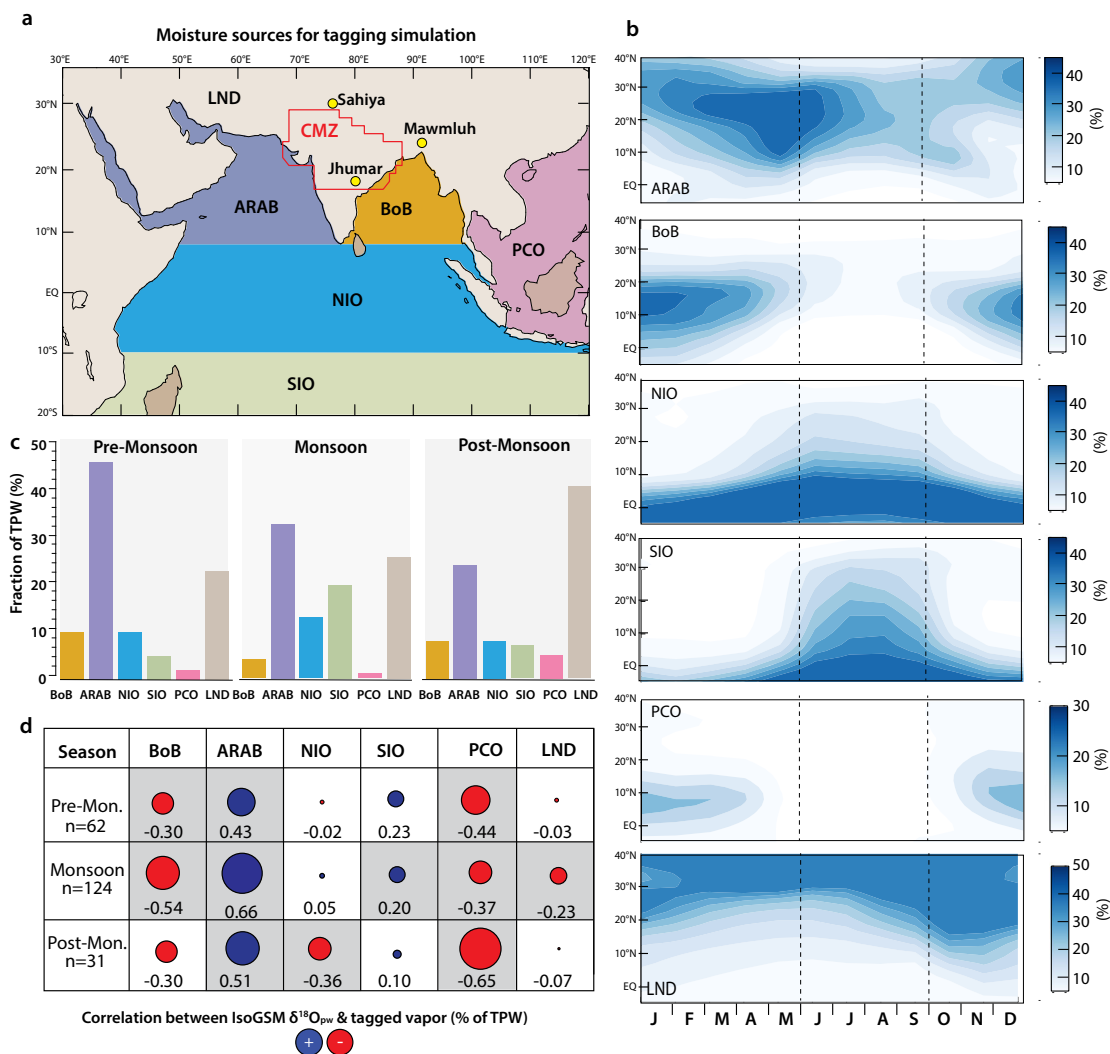


Fig. 1 Results from the IsoGSM2 tagging simulation. **a** Schematic representation of moisture source regions considered in this study (color-coded by names: the Arabian Sea, Red Sea, and the Gulf of Oman (ARAB), Bay of Bengal (BoB), northern Indian Ocean (10°N to 10°S (NIO), southern Indian Ocean (10°S to 20°S (SIO), land surfaces (as shown) (LND), and the western part of the Pacific Ocean (as shown) (PCO). Locations of the speleothem $\delta^{18}\text{O}$ records discussed in the text are marked by yellow circles. The core monsoon zone (CMZ, approximately from 18°N, 28°N, and 69°E, 89°E) is depicted by a polygon. **b** Hovmöller diagram showing the seasonal evolution of tagged vapor as a fraction of total precipitable water (TPW) (%) from each source region (longitudinally averaged between 70°E and 94°E) and spanning between -5°S and 40°N. The June to September monsoon season is highlighted by dotted black lines. **c** Histograms showing relative contributions of each vapor source (%) to TPW averaged over the CMZ for pre-monsoon (April–May, MAM), monsoon (June–September, JJAS), and post-monsoon (September–October, SO) seasons. **d** Correlations between IsoGSM2³⁸ simulated monthly anomalies of oxygen isotopic composition of precipitable water ($\delta^{18}\text{O}_{\text{pw}}$) and fractional moisture (%) for each vapor source over the CMZ during pre-monsoon, monsoon, and post-monsoon seasons (circles). Monthly anomalies were calculated by removing the long-term climatological mean (1979–2010) for each calendar month of the pre-monsoon (April–May), monsoon (June through September), and post-monsoon (October) seasons from each month’s individual value. The circles’ sizes are proportional to the Pearson correlation coefficients (r). The shaded boxes indicate values that are statistically significant ($P < 0.05$ one-tailed, t test; after accounting for autocorrelation). The period of the analysis is from 1979 to 2010.

averaged from 70°E to 94°E) from each tagged region between -5°S to 40°N are illustrated by a Hovmöller diagram (Fig. 1b). During the pre-monsoon season (April–May), moisture contributions to the CMZ are dominated by the ARAB (~50%) and LND source regions (i.e., recycled vapor originating from land surfaces (~20%)) (Fig. 1b, Supplementary Fig. 7). Between late May and early June, contributions from the NIO and SIO abruptly increases over the CMZ marking the intensification of the LLJ, with the SIO exhibiting the largest relative increase with respect to the pre-monsoon level (Fig. 1b and Supplementary Fig. 7). The JJAS climatological moisture contribution to the CMZ and other sink regions are dominated by the ARAB (~40%), LND (~26%), and SIO (2–0%) (Fig. 1b and Supplementary

Fig. 7), peaking in the early (June), late (September), and mid (July–August) part of the monsoon season, respectively (Supplementary Fig. 8a). Between late August and early October, as the ISM withdraws, the relative moisture contributions from the ARAB, NIO, and SIO decrease whereas the contribution from the LND increases sharply (~45%) over the CMZ (Fig. 1b and Supplementary Fig. 7). Linear correlations between the de-seasoned anomalies of IsoGSM2 simulated monthly isotopic composition of precipitable water ($\delta^{18}\text{O}_{\text{pw}}$) and moisture contributions from each tagged source region over the CMZ and other sink regions are summarized in Fig. 1 and Supplementary Fig. 7, respectively. The correlation analysis for the JJAS season indicates the $\delta^{18}\text{O}_{\text{pw}}$ exhibits modest positive and negative relationships with the

ARAB ($r \sim 0.6$) and LND ($r \sim -0.3$) over the CMZ as well for the other sink regions (Supplementary Fig. 7).

In summary, the following key observations from our tagging simulation are noteworthy: (1) contributions from the ARAB, SIO, and LND (i.e., local recycling) tagged regions are important moisture sources of ISM precipitation in the early, mid, and late monsoon season, respectively. These results are in agreement with those estimated within the framework of Lagrangian dispersion models, although the boundaries of the source regions and their relative importance vary among studies^{46,50–52}. (2) From a climatological perspective, moisture contribution from the BoB tagged region is not an important source of JJAS precipitation over much of continental India (except over northeast India). This finding, however, does not contradict the notion that a significant portion of the moisture is transported from the monsoon's southeasterly circulation and the LPS originating from the BoB because the transported moisture may have origins from other sources⁵³. (3) JJAS moisture contributions from ARAB and LND significantly influence the $\delta^{18}\text{O}_{\text{pw}}$ and $\delta^{18}\text{O}_{\text{p}}$ over the Indian subcontinent.

Moisture contributions during weak and strong monsoon years. We used composite analysis to examine relative changes in moisture contributions from each tagged source over the Indian subcontinent during the 'weak and strong' monsoon years. The weak (1982, 1987, 2002, 2004, and 2009) and strong (1983, 1988, and 1994) years are identified as departures of one standard deviation from the All-India Rainfall (AIR) mean (~ 850 mm) between 1979 and 2010. The AIR is an area-weighted mean summer monsoon rainfall index based on a homogeneous rainfall data set of 306 rain gauges in India⁵⁴ and is widely considered as a reliable index of summer monsoon activity over the Indian region (e.g., ref. 24).

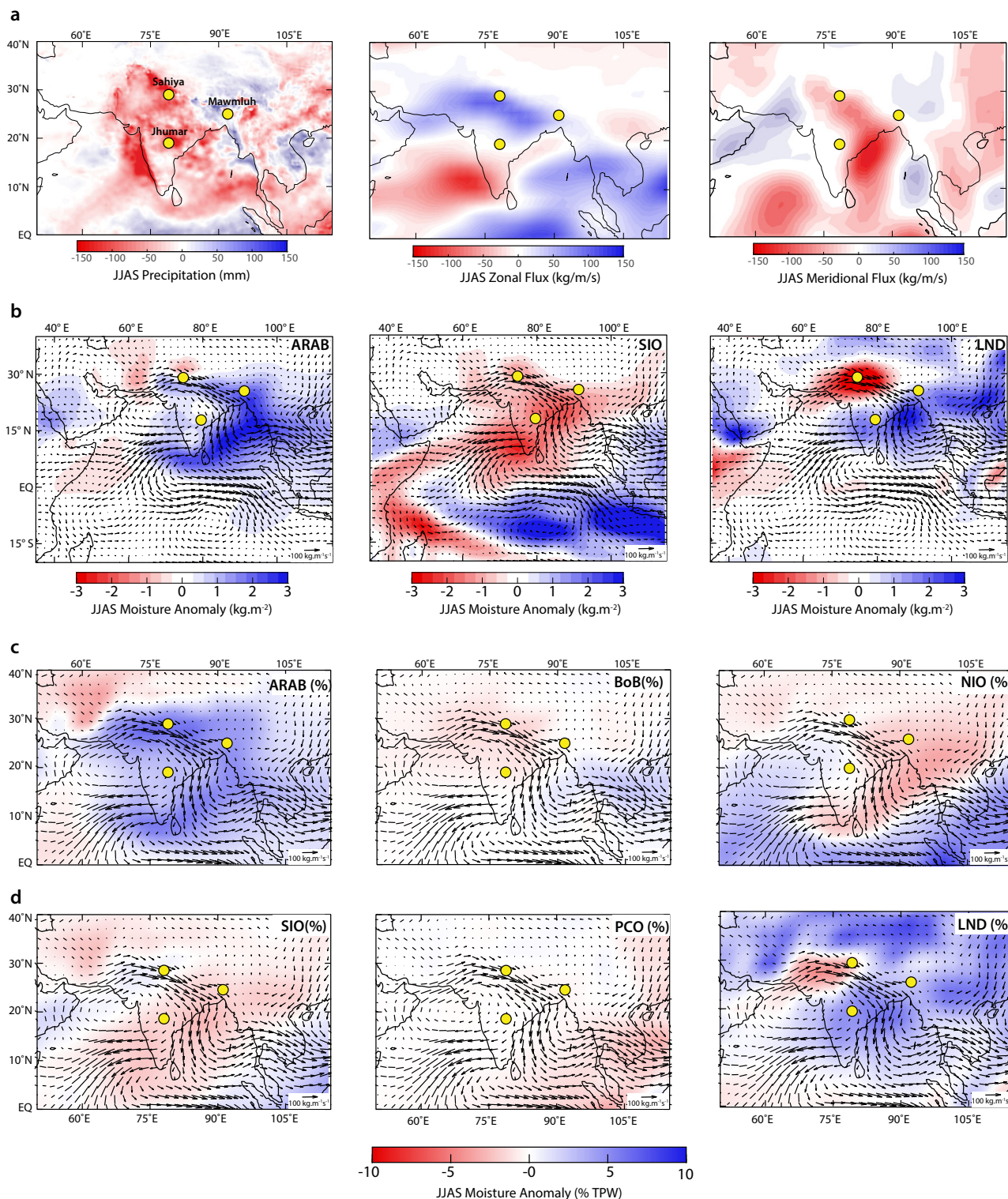
The differences between the weak and strong composites of JJAS precipitation and vertically integrated moisture flux (the sign of those differences is indicative of a weaker monsoon) highlight the following key features (Fig. 2a). The weak monsoon years are characterized by (i) negative precipitation anomalies over much of continental India except over northeast, northern BoB, and the coastal Myanmar regions; (ii) reduced vertically integrated zonal moisture flux along the climatological axis of the LLJ over the Arabian Sea, compensated by anomalously enhanced northwest-southeast trending zonal moisture flux across north India (with its core at $\sim 25^\circ\text{N}$) and near the equator; (iii) negative meridional moisture flux anomalies, particularly east of 75°E over continental India. During the weak monsoon years, the moisture originating from the ARAB tagged region converges over northeast India and BoB due to the anomalous moisture flux and low-level circulation⁵⁵. On the other hand, moisture contribution from the SIO is substantially reduced over continental India and all along the LLJ. There is also a marked reduction in recycled moisture over north India but a large increase over the BoB and southeast Asia during the weak monsoon years (Fig. 2b). In addition, the moisture contributions from the BoB, NIO, and PCO regions are reduced to a varying degree over continental India. It is important to note that Fig. 2b highlights the spatial patterns of moisture contributions from each tagged region on a standalone basis. However, to assess how the $\delta^{18}\text{O}_{\text{pw}}$ and $\delta^{18}\text{O}_{\text{p}}$ vary during the weak and strong monsoon years, it is more instructive to examine the relative changes in moisture contribution ratio. When viewed in this context, the spatial patterns of moisture contribution ratios from the ARAB and LND during the weak monsoon years are uniformly higher over continental India (except over northwest India in case of LND), and lower for all other moisture sources to the TPW (Fig. 2c). These spatial

patterns can be primarily attributed to a shifting balance of ARAB and LND moisture contribution between the weak and strong monsoon years. The higher values of ARAB over the Indian subcontinent during the weak years are mirrored by substantially enriched $\delta^{18}\text{O}_{\text{pw}}$ and $\delta^{18}\text{O}_{\text{p}}$ (Supplementary Fig. 8b) across the ISM domain, which can be attributed to the higher prevalence of isotopically enriched moisture from the proximal ARAB source region.

Interannual variability of moisture contributions, precipitation, and isotopes. We further examined how variations in moisture contributions from ARAB and LND, which show the largest change between weak and strong monsoon years (Fig. 2c), relate to interannual changes in the ISM precipitation and its $\delta^{18}\text{O}_{\text{pw}}$ and $\delta^{18}\text{O}_{\text{p}}$. This is approached by examining the spatial pattern of correlation coefficients between the ARAB and LND with precipitation amount and $\delta^{18}\text{O}_{\text{p}}$ at each grid cell as well as through comparisons of their time series values averaged over a large rectangular-shaped region over continental India (Fig. 3). Here, we used IsoGSM2 simulated precipitation for this analysis, however, the results of this study are not sensitive to the choice of precipitation dataset (Supplementary Fig. 9). Spatial correlation analysis indicates an east–west dipole like-structure, where the JJAS moisture contributions from ARAB are negatively and positively correlated with precipitation amount west and east of 85°E , respectively (Fig. 3a). This spatial pattern is qualitatively similar to the spatial pattern of precipitation anomalies during the weak minus strong monsoon years (Fig. 2a). On the other hand, the spatial pattern of correlations between ARAB (%) and $\delta^{18}\text{O}_{\text{p}}$ at each grid cell are uniformly positive east of 64°E longitude (Supplementary Fig. 10). These observations suggest that during weak monsoon years, a northwest-southeast trending band of anomalously enhanced zonal moisture flux exports ^{18}O enriched moisture from the ARAB source region across the Indian subcontinent and into Southeast Asia and Southern China (Fig. 2a and Supplementary Fig. 1). Over continental India (west of 85°E) time-series comparisons show that precipitation amount is negatively ($r \sim -0.5$) correlated with the ARAB contributions, $\delta^{18}\text{O}_{\text{p}}$ and $\delta^{18}\text{O}_{\text{pw}}$ (Fig. 3c) whereas the ARAB contributions are positively correlated ($r \sim 0.7$) with $\delta^{18}\text{O}_{\text{p}}$ and $\delta^{18}\text{O}_{\text{pw}}$ (Supplementary Fig. 10a). These results are supported by a multivariate empirical orthogonal function (MV-EOF)⁵⁶ analysis using the seasonal mean of JJAS ARAB and precipitation fields (Supplementary Figure 10c–d). The MV-EOF analysis extends conventional EOF by extracting coupled patterns of variability among multiple fields.

The first mode of MV-EOF using the detrended and seasonal mean (normalized by its standard deviation) data illustrates a clear inverse relationship between the ARAB (%) and precipitation over the Indian subcontinent, explaining $\sim 26\%$ of the shared covariance.

The relationships between moisture contributions from LND with precipitation amount, $\delta^{18}\text{O}_{\text{p}}$ and $\delta^{18}\text{O}_{\text{pw}}$ for the mid-to-late part of the monsoon season (AS = August to September) suggests the LND contributions during AS are positively (Fig. 3b) and negatively (Supplementary Fig. 10b) correlated with precipitation amount and $\delta^{18}\text{O}_{\text{p}}$ and $\delta^{18}\text{O}_{\text{pw}}$, respectively over the Indian subcontinent (west 85°E longitude). These observations suggest that higher precipitation amounts during the strong monsoon years lead to greater transpired moisture flux and vice versa. It is interesting to note that IsoGSM2 simulates strong negative correlations (~ -0.7) between moisture contributions from LND with the $\delta^{18}\text{O}_{\text{p}}$ and $\delta^{18}\text{O}_{\text{pw}}$ over continental India, which act to strengthen the inverse relationship between the precipitation amount and $\delta^{18}\text{O}_{\text{p}}$ driven by moisture contributions from the



ARAB. The negative relationship between LND and $\delta^{18}\text{O}_p$ (and $\delta^{18}\text{O}_{pw}$) likely arises due to the waning and waxing influence of moisture contributions from the ARAB and LND during the mid and late part of the monsoon season.

In sum, our analysis suggests that the interannual variability in $\delta^{18}\text{O}_p$ and $\delta^{18}\text{O}_{pw}$ over the ISM domain during the monsoon season is influenced by variations in the moisture contributions from the ARAB and terrestrial recycling. During weak monsoon years, the anomalous increase in zonal moisture flux via a northward shifted LLJ over the Arabian Sea and continental India

serves as a conduit for transporting ^{18}O enriched moisture from the ARAB source region across a northwest-southeast trending region that extends from the Arabian Peninsula to the southeast Asia (Supplementary Fig. 11). These model-based inferences are also supported by the positive correlations of JJAS zonal moisture flux anomalies with the observational monthly $\delta^{18}\text{O}_p$ data from the GNIP sites located within this band (Supplementary Fig. 11). Together, the model-instrumental observations suggest that proxy records of $\delta^{18}\text{O}_p$ from sites situated within this corridor of anomalous moisture flux during weak monsoon years are

Fig. 2 Weak minus strong JJAS composites of climatological fields and “tagged” moisture anomalies. **a** JJAS mean precipitation anomalies from the European Centre Medium-Range Weather Forecasts Reanalysis Fifth generation (ERA-5)⁷¹ (left), vertically integrated zonal flux anomalies (middle), and meridional moisture flux anomalies (right) from ERA-5⁷¹ (shaded). **b** JJAS moisture anomalies from ARAB (left), SIO (middle), and LND (left). **c, d** JJAS moisture (% TPW) (shaded) from ARAB (left), BoB (middle), NIO (right), SIO (left), PCO (middle), LND regions (right) are superimposed by simulated vertically integrated moisture flux anomalies over the same period (1979–2010). Circles in all panels mark the locations of the cave records discussed in the text. The strong (1983, 1988, and 1994) and weak (1982, 1987, 2002, 2004, and 2009) monsoon seasons are defined as positive (negative) departures of one standard deviation from the mean of All India Rainfall⁵⁴. The weak monsoon years are characterized by (i) negative precipitation anomalies over much of continental India except over northeast, northern BoB, and the coastal Myanmar regions; (ii) reduced vertically integrated zonal moisture flux along the climatological axis of the LLJ over the Arabian Sea, compensated by anomalously enhanced northwest-southeast trending zonal moisture flux across north India (with its core at -25°N) and near the equator; (iii) negative meridional moisture flux anomalies, particularly east of 75°E over the Indian subcontinent.

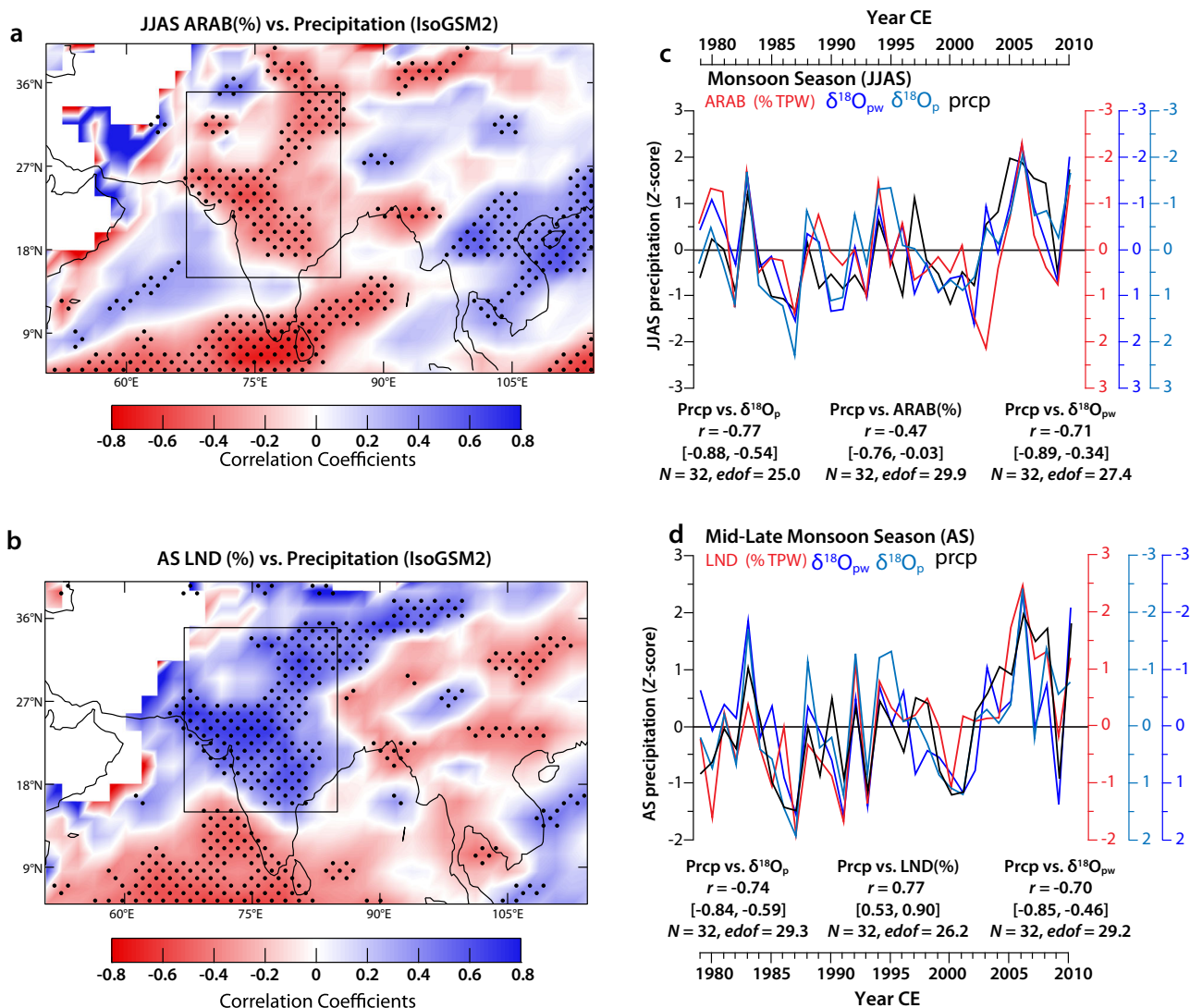


Fig. 3 Spatial correlation fields and time-series comparisons. **a** Correlations between June and September (JJAS) IsoGSM2 simulated ARAB (% TPW) and precipitation amount at each grid cell. The correlation was performed after removing the climatological mean and trend from data (**b**) same as (**a**) but for LND (% TPW) vs. August to September (AS) precipitation amount. The black rectangle in each panel marks the region used for extracting time-series comparisons in panels (**c**) and (**d**). Stippling indicates regions of significant correlations at 95% significance level obtained after accounting for serial correlations and followed by the application of false discovery rate (FDR)⁶⁷ procedure with a 5% threshold (see “Methods”). FDR is the expected proportion of rejected hypotheses when the null hypothesis is actually true for those tests. **c** Z-score transformed time-series comparisons between the JJAS precipitation amount (black), ARAB (% TPW) (red), $\delta^{18}O_p$ (cyan), and $\delta^{18}O_{pw}$ (blue) for 1979–2010. Timeseries for all four variables represent averaged values extracted from a rectangular-shaped region over the Indian subcontinent marked by rectangles in panels (**a**) and (**b**). All vertical axes (right) are reversed and color-coded by variables names. **d** Same as **c** but for August to September precipitation and LND (%) moisture source. The vertical axes for $\delta^{18}O_p$ and $\delta^{18}O_{pw}$ are reversed. The Pearson correlation coefficients (r) with 95% confidence intervals (CI) are shown in each panel. The 95% CI is derived from pairwise moving-block bootstrap resampling ($N = 2000$) and calibration that account for serial autocorrelation in data^{64,65} (see “Methods”).

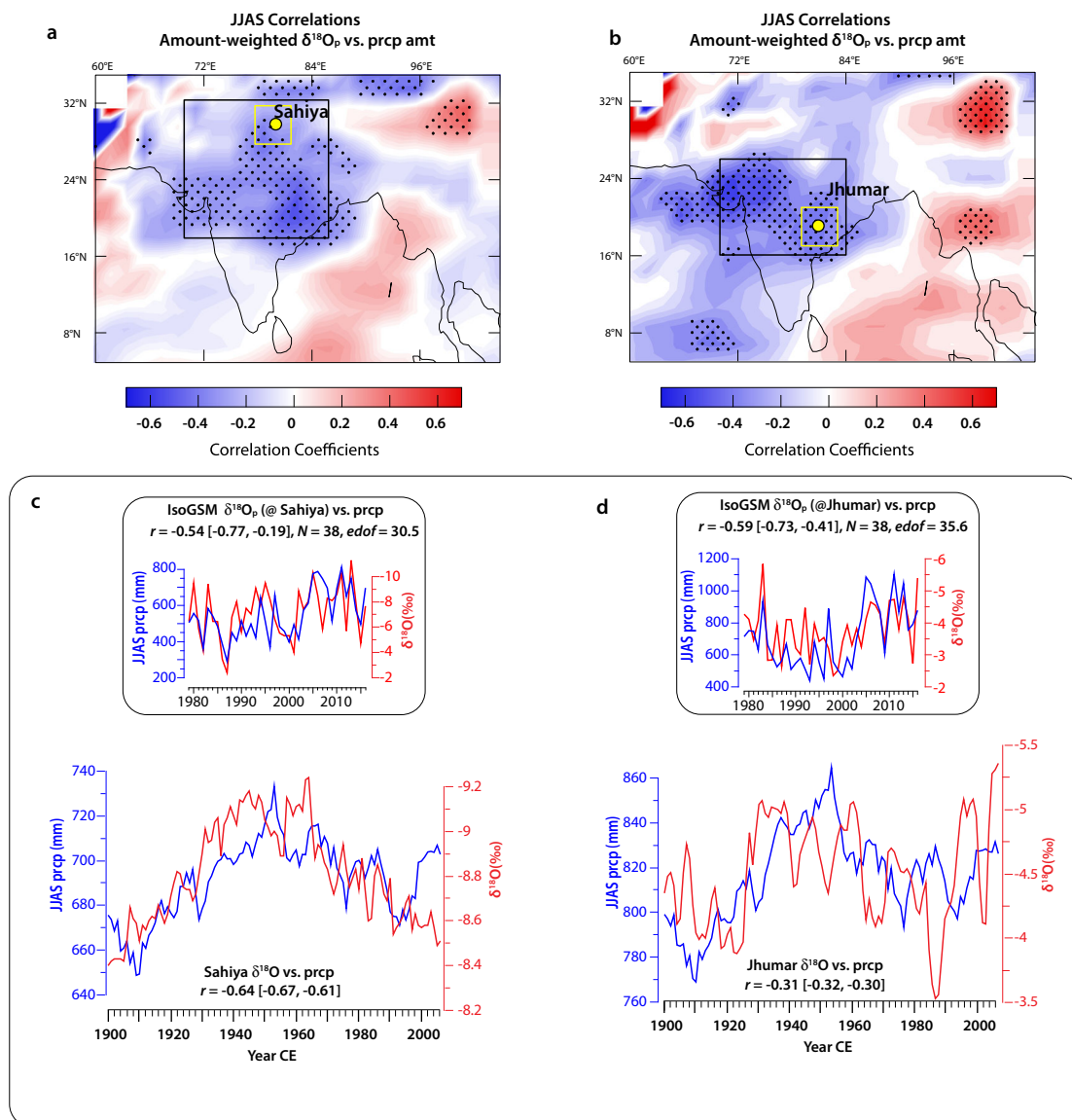


Fig. 4 Spatial correlation fields and time-series comparisons. **a** Correlations between IsoGSM2³⁸ simulated JJAS $\delta^{18}\text{O}_p$ extracted from a $4^\circ \times 4^\circ$ region around Sahiya cave (yellow square) and model-simulated precipitation amount at all other grid points. The correlation was performed after removing the climatological mean and trend from the data. Stippling indicates regions of significant correlations at a 95% significance level obtained after accounting for serial correlations in data at each grid point followed by the application of FDR⁶⁷ procedure with a 5% threshold (see “Methods”). FDR is the expected proportion of rejected hypotheses when the null hypothesis is actually true for those tests. The black rectangle (17°N – 32°N and 70°E – 82°E) demarcates the region from where precipitation amount was extracted for time-series comparisons in panel (c). **b** Same as **a** but for the Jhumar cave⁵⁷ region. Black rectangle demarcates (16°N – 26°N and 70°E – 84°E) the region from where precipitation amount is extracted for time-series comparisons in panel (d). **c** Timeseries comparison between the speleothem $\delta^{18}\text{O}$ from Sahiya cave²⁶ with an 11-year smoothed JJAS precipitation data extracted from the region shown in panel **b** for 1901–2006. The precipitation data is from the Global Precipitation Climatology Centre version-5 (GPCC)⁷². Inset (black rectangle, this study) shows a comparison between the IsoGSM2 simulated $\delta^{18}\text{O}_p$ and precipitation amount for JJAS for 1979–2017. **d** Same as **c** but for the Jhumar speleothem $\delta^{18}\text{O}$ ⁵⁷. The Pearson correlation coefficient (r) with 95% CI is shown in each panel. The 95% CI was derived from pairwise moving-block bootstrap resampling ($N = 2000$) and calibration that account for autocorrelation in data^{64,65} (“Methods”).

particularly well-suited for reconstructing the ISM variability (Fig. 1 and Supplementary Fig. 11).

Discussion

The results from our study have implications for interpreting the existing speleothem oxygen isotope records from the region (Fig. 1 and Supplementary Note 1). The IsoGSM2³⁸ simulated JJAS $\delta^{18}\text{O}_p$ data extracted from the model’s grid cells enclosing the speleothem sites in north and central India (Supplementary Fig. 1) exhibit a moderate inverse relationship with regional

precipitation amount over the land and the oceanic regions upstream of the 85°E longitude (Fig. 4). Similarly, the time-series comparisons of the published speleothem $\delta^{18}\text{O}$ profiles from Jhumar and Sahiya caves^{26,57} with smoothed instrumental precipitation data (~1901–2006) also exhibit inverse relationships (Fig. 4), which are broadly consistent with the model simulated inverse $\delta^{18}\text{O}_p$ –precipitation relationship. However, the regional precipitation amount at both cave sites can only explain, at the best, up to half of the isotopic variance in $\delta^{18}\text{O}_p$ and speleothem $\delta^{18}\text{O}$, suggesting that a large fraction of $\delta^{18}\text{O}_p$ (and consequently, speleothem $\delta^{18}\text{O}$) variability also stem from changes in moisture

source dynamics and circulation as well as from other processes such as organized convection over the ocean moisture source regions, rainout during the moisture transport, and local convection^{13,14,17,49,58}. It is also important to note that the inverse $\delta^{18}\text{O}_p$ -precipitation relationships observed in the simulated and proxy data do not necessarily stem from the classic “amount effect” as previously suggested^{23–25} but rather from the relative changes in moisture contributions and attendant changes in circulation. These observations imply that the speleothem $\delta^{18}\text{O}$ records from north and central India can be broadly interpreted in a framework of overall changes in the upstream circulation, moisture source dynamics, and regional precipitation intensity. Reliable interpretation of speleothem data, however, must also take into account the various cave and karst-specific processes, which can modify the $\delta^{18}\text{O}_p$ signal to a varying degree (e.g., ref. 26).

While our analysis with IsoGSM2 tagging simulation data primarily elucidates the potential mechanisms of $\delta^{18}\text{O}_p$ inter-annual variability, it can provide potential insights to understanding the large amplitude and low-frequency changes observed in various ISM speleothem records on multidecadal-to-millennial-and-orbital timescales. For example, a large increase in $\delta^{18}\text{O}$ (~6–8‰) during the millennial-scale cold climate events is a striking feature in some speleothem records from India^{20,21}, which is not easily explained within the framework of modern climatological ISM dynamics. Observational data show that a large fraction of ISM intraseasonal variability is tied to quasi-periodic episodes of active and break spells—two distinct oscillatory modes of monsoon that have radically different synoptic-scale circulation and precipitation patterns^{40,48}. A characteristic feature of the break phase is large-scale negative precipitation anomalies over much of continental India that are accompanied by anomalously positive zonal moisture transport with its core centered at ~25°N at the expense of its climatological position at ~15°N (Supplementary Fig. 1d)—features that are reminiscent of the weak minus strong years as discussed above. The difference of the break minus active composites of the amount weighted simulated $\delta^{18}\text{O}_p$ from IsoGSM2³⁸ show positive $\delta^{18}\text{O}_p$ anomalies of up to 6–8‰ over a wide swath of region extending from northwest India to southeast Asia that can be attributed to higher moisture contributions from the ARAB source region (Supplementary Fig. 12). Admittedly speculative, a scenario that calls for preferential locking of the ISM circulation into a “break mode” during the millennial cold events could potentially explain a large portion of the observed increase in $\delta^{18}\text{O}$ values in the speleothem records^{20,21} in conjunction with changes in the $\delta^{18}\text{O}_p$ resulting from other processes such as variations in the global ice volume, sea level, and regional temperatures. The same mechanism but working on shorter timescales (i.e., via the more frequent asymmetric occurrence of break spells in each monsoon season)²⁴ can also potentially explain the protracted episodes of anomalously enriched $\delta^{18}\text{O}$ values reported from some speleothem records from India^{23–27}. On orbital timescales, recent simulations with an Earth System model with water isotope tracers³⁶ indicate reduced ISM rainfall, heavier $\delta^{18}\text{O}_p$, and increased moisture contributions from proximal sources (e.g., the Arabian Sea and the Red Sea) to the Indian subcontinent during precession maxima (low Northern Hemisphere summer insolation) and vice versa³⁶ thus, supporting the idea that $\delta^{18}\text{O}_p$ variations over the Indian subcontinent reflect large-scale changes in circulation, moisture sources, and rainfall amounts.

Methods

We used Isotope-incorporated Global Spectral Model version 2 (IsoGSM2)³⁸, which is a version of the Scripps Experimental Climate Prediction Center’s global spectral model. The atmosphere in IsoGSM2 has a horizontal resolution of ~200

km (T62) with 28 vertical levels. The model is forced with prescribed sea surface temperatures and sea ice conditions from the optimal interpolation daily dataset provided by the National Centers for Environmental Prediction (NCEP)⁵⁹. The default land surface scheme is the Noah model⁶⁰. The IsoGSM2 applies a global downscaling technique, which nudges temperature and wind speed (at scales larger than 1000 km) toward the National Center for Environmental Prediction Reanalysis 2 (NCEP R2)^{38,61}. The nudging (performed at every 6 h for all sigma levels) provides dynamical constraints to the simulated atmospheric circulation and is directly comparable with the observations. In IsoGSM, most isotopic fractionations are assumed to occur at thermodynamic equilibrium, except for open water evaporation, condensation in supersaturation conditions (vapor to ice), raindrop re-evaporation, and air-rain isotopic exchange, where kinetic fractionation occurs. IsoGSM2 assumes no fractionation when water evaporates over land. All precipitation is fully mixed into a simple single bucket-type model for treatment of soil water isotopes, which provides storage of all water species, and consequently, the isotope ratio of evapotranspiration is assumed to be the same as stored values.

Simulated precipitation from IsoGSM2 broadly replicates the observations over South Asia although it underestimates precipitation amount over northwest India, Indo-Gangetic plains, and the Western Ghats and overestimates over the BoB and coastal Myanmar (Supplementary Fig. 2). IsoGSM2 simulated $\delta^{18}\text{O}_p$ has been previously validated with observational data from South Asia at event based²⁵, daily^{31,49}, and monthly timescales²⁶. Here, we further validate the IsoGSM2 simulated data with some of the longest daily (Supplementary Table 1) and monthly GNIP $\delta^{18}\text{O}_p$ data from several additional sites located in south and southeast Asia. The model can reproduce the annual cycle and interannual variability in $\delta^{18}\text{O}_p$ with high fidelity for GNIP stations at Dhaka, New Delhi, Bangkok, and Kunming (Supplementary Figs. 3–5). In the tracer mode, IsoGSM2 can track a given moisture mass back to its last time at sea level by setting the surface evaporative fractionation factor to 1 for the target region (and 0 for all other regions) and by turning off all the other isotopic fractionation in the atmosphere. The evaporated water is marked by its origin with a tag. The tagged vapor once added to the atmosphere is allowed to undergo the same atmospheric hydrological cycle as normal water vapor until it leaves the atmosphere as precipitation^{49,62,63}. The tagged simulation output (1979–2010) was generated at daily intervals and interpolated into 17 vertical pressure levels and monthly averaged.

We used the least-squares linear regression to determine linear Pearson correlation coefficients between independent and dependent variables. Confidence intervals of Pearson correlation coefficients were determined using a pairwise moving-block bootstrap method with an average block length proportional to the estimated data autocorrelation using a PearsonT3 software⁶⁴. This method preserves the serial dependence of time series and provides the corrected 95% confidence intervals that are valid in the presence of autocorrelation^{64,65}. The coverage accuracy is increased by applying calibration to standard error-based bootstrap Student’s *t* confidence interval. The effective degree of freedom (EDOF) was estimated by the following equation

$$\text{EDOF} = N * \frac{1 - (r1 * r2)}{1 + (r1 * r2)}$$

where *N* denotes the length of time series and *r1* and *r2* are lag-one autocorrelations of each timeseries⁶⁶.

Unlike pairwise comparisons (where the significance level α —the probability of falsely rejecting the null hypothesis of zero correlation provides the basis of hypothesis testing), the statistical significance of field correlations (example, Figs. 3 and 4 in the main text and other supplementary figures) requires conducting multiple tests at different locations simultaneously. Increasing numbers of simultaneous tests (in accordance with increasing resolution of grid points) may lead to a higher number of correlations that may be incorrectly deemed as “significant”—the test multiplicity problem. We applied the false discovery rate (FDR) procedure⁶⁷ to control the proportion ($q = 5\%$) of erroneously rejected null hypotheses using a MATLAB code⁶⁸, where *q* guarantees that 5% or fewer of the locations where the null hypothesis is rejected are false detections. FDR generally provides a more powerful method for correcting for multiple comparisons (e.g., refs. 69,70) than procedures like Bonferroni correction that provide strong control of the family-wise error rate (i.e., the probability that one or more null hypotheses are mistakenly rejected).

Data availability

The simulation data from isotope-incorporated Global Spectral Model version 2 (IsoGSM2) are available at <http://isotope.iis.u-tokyo.ac.jp/~kei/tmp/isogsm2/>. Moisture tagging simulation data are available at the Zenodo repository at <https://doi.org/10.5061/dryad.4b8gtht7>. Data are also available upon request from the corresponding authors. The All-India Rainfall (AIR) data from the Indian Institute of Tropical Meteorology (IITM) meteorological is available at <https://mol.tropmet.res.in/>. The precipitation isotope data by Global Network of Isotopes in Precipitation (GNIP) stations are available at <https://nuclues.iaea.org/wiser>. The Global Precipitation Climatology Centre (GPCC) version 7 precipitation data is available at <https://psl.noaa.gov/data/gridded/data.gpcc.html>. The Global Precipitation Climatology Project (GPCP) version 2.3 data are available at <https://psl.noaa.gov/data/gridded/data.gpcp.html>. The Climatic Research Unit Timeseries (CRU-TS) version 4.0 data are available at <https://crudata.uea.ac.uk/cru/data/hr/>. The moisture flux divergence, vertically integrated moisture flux, and precipitation

data from European Centre for Medium-Range Weather Forecasts reanalysis (ERA-5) are available at <https://cds.climate.copernicus.eu/>.

Code availability

The MATLAB code for estimating the FDR⁶⁸ is available at <https://www.mathworks.com/matlabcentral/fileexchange/71734-fdr>.

Received: 10 December 2020; Accepted: 15 April 2021;

Published online: 20 May 2021

References

- Maher, B. A. Holocene variability of the East Asian summer monsoon from Chinese cave records: a re-assessment. *Holocene* **18**, 861–866 (2008).
- Clemens, S. C., Prell, W. L. & Sun, Y. Orbital-scale timing and mechanisms driving Late Pleistocene Indo-Asian summer monsoons: reinterpreting cave speleothem $\delta^{18}\text{O}$. *Paleoceanography* **25**, 1–19 (2010).
- Pausata, F. S. R., Battisti, D. S., Nisancioglu, K. H. & Bitz, C. M. Chinese stalagmite $\delta^{18}\text{O}$ controlled by changes in the Indian monsoon during a simulated Heinrich event. *Nat. Geosci.* **4**, 474–480, (2011).
- Caley, T., Roche, D. M. & Renssen, H. Orbital Asian summer monsoon dynamics revealed using an isotope-enabled global climate model. *Nat. Commun.* **5**, 1–6 (2014).
- Cheng, H. et al. The Asian monsoon over the past 640,000 years and ice age terminations. *Nature* **534**, 640–646 (2016).
- Zhang, H. et al. East Asian hydroclimate modulated by the position of the westerlies during Termination I. *Science* **362**, 580–583 (2018).
- Chiang, J. C., Herman, M. J., Yoshimura, K. & Fung, I. Y. Enriched East Asian oxygen isotope of precipitation indicates reduced summer seasonality in regional climate and westerlies. *Proc. Natl Acad. Sci. USA*. 14745–14750 (2020).
- Wang, Y.-J. et al. A high-resolution absolute-dated late Pleistocene monsoon record from Hulu Cave, China. *Science* **294**, 2345–2348 (2001).
- Yuan, D. et al. Timing, duration, and transitions of the last interglacial Asian monsoon. *Science* **304**, 575–578 (2004).
- Werner, M., Langebroek, P. M., Carlsen, T., Herold, M. & Lohmann, G. Stable water isotopes in the ECHAM5 general circulation model: toward high-resolution isotope modeling on a global scale. *J. Geophys. Res.* **116** (2011).
- Yoshimura, K. Stable water isotopes in climatology, meteorology, and hydrology: a review. *J. Meteorol. Soc. Jpn. Ser. II* **93**, 513–533 (2015).
- Comas-Bru, L. et al. Evaluating model outputs using integrated global speleothem records of climate change since the last glacial. *Clim. Past* **15**, 1557–1579 (2019).
- Yang, H., Johnson, K. R., Griffiths, M. & Yoshimura, K. Interannual controls on oxygen isotope variability in Asian monsoon precipitation and implications for paleoclimate reconstructions. *J. Geophys. Res.* **121**, 8410–8428 (2016).
- Cai, Z., Tian, L. & Bowen, G. J. Spatial-seasonal patterns reveal large-scale atmospheric controls on Asian Monsoon precipitation water isotope ratios. *Earth Planet. Sci. Lett.* **503**, 158–169 (2018).
- LeGrande, A. & Schmidt, G. Sources of Holocene variability of oxygen isotopes in paleoclimate archives. *Clim. Past* **5**, 441–455 (2009).
- Maher, B. A. & Thompson, R. Oxygen isotopes from Chinese caves: records not of monsoon rainfall but of circulation regime. *J. Quat. Sci.* **27**, 615–624 (2012).
- Ruan, J., Zhang, H., Cai, Z., Yang, X. & Yin, J. Regional controls on daily to interannual variations of precipitation isotope ratios in Southeast China: implications for paleomonsoon reconstruction. *Earth Planet. Sci. Lett.* **527**, 115794 (2019).
- Zhang, H. et al. The Asian summer monsoon: teleconnections and forcing mechanisms—a review from Chinese speleothem $\delta^{18}\text{O}$ records. *Quaternary* **2**, 26 (2019).
- Kaushal, N. et al. The Indian summer monsoon from a speleothem $\delta^{18}\text{O}$ perspective—a review. *Quaternary* **1**, 29 (2018).
- Dutt, S. et al. Abrupt changes in Indian summer monsoon strength during 33,800 to 5500 years BP. *Geophys. Res. Lett.* **42**, 5526–5532 (2015).
- Kathayat, G. et al. Indian monsoon variability on millennial-orbital timescales. *Sci. Rep.* **6**, 24374 (2016).
- Cheng, H. & Edwards, R. L. Atmospheric $^{14}\text{C}/^{12}\text{C}$ changes during the last glacial period from Hulu Cave. *Science* **362**, 1293–1297 (2018).
- Sinha, A. et al. A 900-year (600 to 1500 AD) record of the Indian summer monsoon precipitation from the core monsoon zone of India. *Geophys. Res. Lett.* **34** (2007).
- Sinha, A. et al. A global context for megadroughts in monsoon Asia during the past millennium. *Quat. Sci. Rev.* **30**, 47–62 (2011).
- Berkelhammer, M. et al. An abrupt shift in the Indian monsoon 4000 years ago. *Geophys. Monogr. Ser.* **198**, 75–87 (2012).
- Sinha, A. et al. Trends and oscillations in the Indian summer monsoon rainfall over the last two millennia. *Nature. Nat. Commun.* **6**, 1–8 (2015).
- Kathayat, G. et al. The Indian monsoon variability and civilization changes in the Indian subcontinent. *Sci. Adv.* **3**, e1701296 (2017).
- Breitenbach, S. F. et al. Strong influence of water vapor source dynamics on stable isotopes in precipitation observed in Southern Meghalaya, NE India. *Earth Planet. Sci. Lett.* **292**, 212–220 (2010).
- Myers, C. G. et al. Northeast Indian stalagmite records Pacific decadal climate change: implications for moisture transport and drought in India. *Geophys. Res. Lett.* **42**, 4124–4132 (2015).
- Deshpande, R., Dave, M., Padhya, V., Kumar, H. & Gupta, S. Water vapour source identification for daily rain events at Ahmedabad in semi-arid western India: wind trajectory analyses. *Meteorol. Appl.* **22**, 754–762 (2015).
- Midhun, M. et al. The effect of monsoon circulation on the stable isotopic composition of rainfall. *J. Geophys. Res.* **123**, 5205–5221 (2018).
- Yoshimura, K., Oki, T., Ohte, N. & KANAIE, S. Colored moisture analysis estimates of variations in 1998 Asian monsoon water sources. *J. Meteorol. Soc. Jpn. Ser. II* **82**, 1315–1329 (2004).
- Ichiyanagi, K., Yoshimura, K. & Yamanaka, M. D. Validation of changing water origins over Indochina during the withdrawal of the Asian monsoon using stable isotopes. *SOLA* **1**, 113–116 (2005).
- Noone, D. & Sturm, C. in *Isoscapes*, 195–219 (Springer, 2010).
- Suvarman, R. et al. The variability of stable isotopes and water origin of precipitation over the Maritime Continent. *SOLA* **9**, 74–78 (2013).
- Tabor, C. R. et al. Interpreting precession-driven $\delta^{18}\text{O}$ variability in the South Asian monsoon region. *J. Geophys. Res.* **123**, 5927–5946 (2018).
- Hu, J., Emile-Geay, J., Tabor, C., Nusbaumer, J. & Partin, J. Deciphering oxygen isotope records from Chinese speleothems with an isotope-enabled climate model. *Paleoceanogr. Paleoclimatol.* **34**, 2098–2112 (2019).
- Yoshimura, K., Kanamitsu, M., Noone, D. & Oki, T. Historical isotope simulation using reanalysis atmospheric data. *J. Geophys. Res.* **113** (2008).
- Midhun, M. & Ramesh, R. Validation of $\delta^{18}\text{O}$ as a proxy for past monsoon rain by multi-GCM simulations. *Clim. Dyn.* **46**, 1371–1385 (2016).
- Joseph, P. & Sijikumar, S. Intraseasonal variability of the low-level jet stream of the Asian summer monsoon. *J. Clim.* **17**, 1449–1458 (2004).
- Goswami, B. & Chakravorty, S. in *Oxford Research Encyclopedia of Climate Science* (2017).
- Krishnamurthy, V. & Ajayamohan, R. Composite structure of monsoon low pressure systems and its relation to Indian rainfall. *J. Clim.* **23**, 4285–4305 (2010).
- Fasullo, J. & Webster, P. J. Hydrological signatures relating the Asian Summer Monsoon and ENSO. *J. Clim.* **15**, 3082–3095 (2002).
- Syed, F. & Hannachi, A. Inter-annual variability of moisture transport over the northern Indian Ocean and South Asian summer monsoon. *Clim. Res.* **75**, 23–31 (2018).
- Neena, J., Dilip, V. & Subramanian, A. *Understanding the Subseasonal Modulation of Moisture Transport over the Indian Monsoon Domain*. (2020).
- Gimeno, L., Drumond, A., Nieto, R., Trigo, R. M. & Stohl, A. On the origin of continental precipitation. *Geophys. Res. Lett.* **37** (2010).
- Gimeno, L. et al. Oceanic and terrestrial sources of continental precipitation. *Rev. Geophys.* **50**, 1–41 (2012).
- Rajeevan, M., Gadgil, S. & Bhate, J. Active and break spells of the Indian summer monsoon. *J. Earth Syst. Sci.* **119**, 229–247 (2010).
- Tanoue, M. et al. Seasonal variation in isotopic composition and the origin of precipitation over Bangladesh. *Progr. Earth Planet. Sci.* **5**, 1–16 (2018).
- Levine, R. C. & Turner, A. G. Dependence of Indian monsoon rainfall on moisture fluxes across the Arabian Sea and the impact of coupled model sea surface temperature biases. *Clim. Dyn.* **38**, 2167–2190 (2012).
- Ordóñez, P., Ribera, P., Gallego, D. & Peña-Ortiz, C. Major moisture sources for Western and Southern India and their role on synoptic-scale rainfall events. *Hydrol. Processes* **26**, 3886–3895 (2012).
- Pathak, A., Ghosh, S., Martinez, J. A., Dominguez, F. & Kumar, P. Role of oceanic and land moisture sources and transport in the seasonal and interannual variability of summer monsoon in India. *J. Clim.* **30**, 1839–1859 (2017).
- Mei, R., Ashfaq, M., Rastogi, D., Leung, L. R. & Dominguez, F. Dominating controls for wetter South Asian summer monsoon in the twenty-first century. *J. Clim.* **28**, 3400–3419 (2015).
- Parthasarathy, B., Munot, A. A. & Kothawale, D. R. All-India monthly and seasonal rainfall series: 1871–1993. *Theor. Appl. Climatol.* **49**, 217–224, (1994).
- Murata, F. et al. Dominant synoptic disturbance in the extreme rainfall at Cherrapunji, Northeast India, based on 104 years of rainfall data (1902–2005). *J. Clim.* **30**, 8237–8251 (2017).
- Wang, B. The vertical structure and development of the ENSO anomaly mode during 1979–1989. *J. Atmos. Sci.* **49**, 698–712 (1992).

57. Sinha, A. et al. The leading mode of Indian summer monsoon precipitation variability during the last millennium. *Geophys. Res. Lett.* **38** (2011).
58. Lekshmy, P., Midhun, M., Ramesh, R. & Jani, R. 18O depletion in monsoon rain relates to large scale organized convection rather than the amount of rainfall. *Sci. Rep.* **4**, 5661 (2014).
59. Reynolds, R. W. et al. Daily high-resolution-blended analyses for sea surface temperature. *J. Clim.* **20**, 5473–5496 (2007).
60. Ek, M. B. et al. Implementation of Noah land surface model advances in the National Centers for Environmental Prediction operational mesoscale Eta model. *J. Geophys. Res.* <https://doi.org/10.1029/2002JD003296> (2003).
61. Yoshimura, K. & Kanamitsu, M. Dynamical global downscaling of global reanalysis. *Mon. Weather Rev.* **136**, 2983–2998 (2008).
62. Buening, N. H., Stott, L., Kanner, L. & Yoshimura, K. Diagnosing atmospheric influences on the interannual 18O/16O variations in western US precipitation. *Water* **5**, 1116–1140 (2013).
63. Wei, Z. et al. Influences of large-scale convection and moisture source on monthly precipitation isotope ratios observed in Thailand, Southeast Asia. *Earth Planet. Sci. Lett.* **488**, 181–192 (2018).
64. Ólafsdóttir, K. B. & Mudelsee, M. More accurate, calibrated bootstrap confidence intervals for estimating the correlation between two timeseries. *Math. Geosci.* **46**, 411–427 (2014).
65. Mudelsee, M. *Climate Timeseries Analysis*. (Springer, Heidelberg, 2013).
66. Bretherton, C. S., Widmann, M., Dymnikov, V. P., Wallace, J. M. & Bladé, I. The effective number of spatial degrees of freedom of a time-varying field. *J. Clim.* **12**, 1990–2009 (1999).
67. Benjamini, Y. & Hochberg, Y. Controlling the false discovery rate: a practical and powerful approach to multiple testing. *Journal of the Royal Statistical Society. J. R. Stat. Soc. Ser. B (Methodol.)* **57**, 289–300 (1995).
68. Gerber M. E. FDR (False Discovery Rate) (<https://www.mathworks.com/matlabcentral/fileexchange/71734-fdr> false-discovery-rate), MATLAB Central File Exchange. Retrieved February 17, 2021 (2021).
69. Ventura, V., Paciorek, C. J. & Risbey, J. S. Controlling the proportion of falsely rejected hypotheses when conducting multiple tests with climatological data. *J. Clim.* **17**, 4343–4356 (2004).
70. Hu, J., Emile-Geay, J. & Partin, J. Correlation-based interpretations of paleoclimate data—where statistics meet past climates. *Earth Planet. Sci. Lett.* **459**, 362–371 (2017).
71. Hersbach, H. et al. The ERA5 global reanalysis. *Q. J. R. Meteorol. Soc.* 1999–2049 (2020).
72. Schneider, U. et al. Evaluating the hydrological cycle over land using the newly-corrected precipitation climatology from the Global Precipitation Climatology Centre (GPCC). *Atmosphere* **8**, 52 (2017).

Acknowledgements

We thank M. Berkelhammer for providing comments on an earlier version of this manuscript. This work was supported by the National Natural Science Foundation of China (NSFC) grants 41888101, 41731174 to H.C. 41703007 to G.K., and 41972186 to H. W. A.S. acknowledges partial support from the CAS PIFI Program (2020VCA0019).

Author contributions

A.S. conceived the project and wrote the paper with G.K. Moisture tagging simulation was conducted by M.T and K.Y. A.S., G.K., H.L., H.Z., and H.C. analyzed the results and all authors commented on the paper.

Competing interests

The authors declare no competing interests.

Additional information

Supplementary information The online version contains supplementary material available at <https://doi.org/10.1038/s43247-021-00165-z>.

Correspondence and requests for materials should be addressed to G.K. or A.S.

Peer review information Primary handling editors: Sze Ling Ho, Joe Aslin

Reprints and permission information is available at <http://www.nature.com/reprints>

Publisher's note Springer Nature remains neutral with regard to jurisdictional claims in published maps and institutional affiliations.



Open Access This article is licensed under a Creative Commons Attribution 4.0 International License, which permits use, sharing, adaptation, distribution and reproduction in any medium or format, as long as you give appropriate credit to the original author(s) and the source, provide a link to the Creative Commons license, and indicate if changes were made. The images or other third party material in this article are included in the article's Creative Commons license, unless indicated otherwise in a credit line to the material. If material is not included in the article's Creative Commons license and your intended use is not permitted by statutory regulation or exceeds the permitted use, you will need to obtain permission directly from the copyright holder. To view a copy of this license, visit <http://creativecommons.org/licenses/by/4.0/>.

© The Author(s) 2021